ESCAP/WMO
Typhoon Committee

Available online at www.sciencedirect.com

ScienceDirect

Tropical Cyclone Research and Review 14 (2025) 384–397

www.keaipublishing.com/tcrr

The role of oceanic parameters in genesis potential indices for enhancing tropical cyclogenesis forecasting in the Bay of Bengal

P. Suneeta [1,*], T.V.S. Udaya Bhaskar [1], E. Pattabhi Rama Rao [1], S.S.V.S. Ramakrishna [2], C.V. Naidu [2]

[1] *Ocean Data Management Group, Indian National Center for Ocean Information Services, MoES, Govt. of India, Hyderabad, India*
[2] *Department of Meteorology and Oceanography, College of Science and Technology, Andhra University, Visakhapatnam, India*

Available online 5 November 2025

Abstract

This study presents an advanced approach for forecasting tropical cyclone genesis, a critical component of disaster preparedness and mitigation for coastal regions prone to extreme weather events. Unlike traditional Genesis Potential Indices (GPIs), which rely solely on atmospheric parameters, we propose a novel GPI framework that integrates both atmospheric (relative vorticity, relative humidity, vertical wind shear, thermal instability) and oceanic variables (Upper Ocean Heat Content [UOHC], Sea Surface Height [SSH]) to enhance predictive skill over the Bay of Bengal (BoB). Building on earlier works, we introduce improved indices GPIS and GPIS1 by incorporating oceanic parameters and evaluate their performance against the existing atmospheric-only index GPIK for four post-monsoon cyclonic events (*Kyant, Bulbul, Bruvi*, and *Mandous*) during 2016–2022. During Cyclone *Bulbul* the highest correlations ($r = 0.94$) were recorded between GPIS and GPIS1, and between GPIK and GPIS, with the lowest RMSE (2.44) between GPIK and GPIS. For Cyclone *Mandous*, GPIK and GPIS1 showed the strongest correlation ($r = 0.96$) and lowest RMSE (1.79), while GPIK-GPIS maintained a good correlation ($r = 0.88$) with an RMSE of 4.68. GPIS1 consistently outperformed the other indices, particularly when paired with GPIK, and detected developing low-pressure systems 3–4 days in advance significantly earlier than the 1-day lead time of the India Meteorological Department's operational GPI. These results highlight the novelty and value of integrating atmospheric and oceanic parameters in GPIs, and underscore the benefits of multi-index analysis for capturing storm-specific variability and improving early identification of cyclogenesis in the BoB during the post-monsoon season.

Key words: Cyclones; Bay of Bengal; Genesis potential index; Post monsoon season; Upper ocean heat content; Sea surface height

1. Introduction

Tropical cyclones are among the most devastating natural disasters, and the Indian subcontinent is particularly vulnerable, facing these extreme weather events during two key periods: April–May (pre-monsoon) and October–December (post-monsoon). The primary driver of cyclone formation is the ocean, which supplies essential heat, moisture, and momentum to fuel these systems. Numerous studies have explored seasonal cyclone activity across various regions, such as Australia (Nicholls, 1984; 1992) and the southern Pacific (Revell and Goulter, 1986). In the North Indian Ocean (NIO), Balachandran and Geetha (2012) developed a statistical model to predict cyclone days, while Gray (1979) identified key conditions for cyclone genesis, including warm sea surface temperatures (≥26.5 °C to a depth of 50 m), an unstable atmosphere, a moist mid-troposphere, a pre-existing surface disturbance, low vertical wind shear and a sufficient Coriolis effect away from the equator. The Bay of Bengal (BoB) experiences nearly four times more cyclones than the Arabian Sea, making India's eastern coastline highly susceptible to cyclone-induced damage such as storm surges, heavy rainfall, and flooding. Recent events, such as Super Cyclone Amphan

* Corresponding author. INCOIS, MoES, Govt. of India, Hyderabad, India.
E-mail address: ponnagantisuneeta@gmail.com (P. Suneeta).
Peer review under the responsibility of Shanghai Typhoon Institute of China Meteorology Administration.

https://doi.org/10.1016/j.tcrr.2025.11.007

(May 2020), have demonstrated the destructive potential of such systems. Various Genesis Potential Index (GPI) studies have attempted to model cyclogenesis (Emanuel, 1987; Roy Bhowmik, 2003; Chu, 2004; Camargo, 2007; Pun et al., 2013). Kotal et al. (2009) developed a GPI for the NIO, which is currently used by the IMD and is primarily based on atmospheric parameters such as relative vorticity, mid-tropospheric humidity, vertical wind shear, and potential intensity. Murakami and Wang (2010) enhanced this by including vertical velocity as additional parameter.

Tropical cyclogenesis over the NIO, particularly in the BoB, is strongly modulated by both atmospheric and oceanic processes. While atmospheric parameters like low-level vorticity, humidity, and vertical wind shear have long been used to assess cyclone potential, recent studies emphasize the importance of oceanic contributions such as Sea Surface Temperature (SST), UOHC and SSH in accurately predicting cyclone formation and intensity. Emmanuel et al. (2021) demonstrated the influence of tropical waves on the genesis of severe cyclonic storm Mora over the NIO. Similarly, Mohan et al. (2022) showed that SST plays a critical role in determining the intensity of extremely severe cyclones such as Fani and Amphan. The impact of ocean-atmosphere coupling and surface roughness on cyclone simulations has also been studied using numerical models like WRF-OML (Nellipudi et al., 2021; Ramakrishna et al., 2019), revealing sensitivity in cyclone representation. Mohanty et al. (2019) further underscored the role of SST in modulating the lifecycle of cyclones in the BoB. Complementary to these findings, Mohapatra et al. (2012) classified cyclone-prone regions of India, aiding in risk assessment and disaster planning. Furthermore, Rao et al. (2019) highlighted the role of soil moisture and land surface feedbacks in maintaining the post-landfall structure of cyclones. These region-specific studies underscore the significance of integrating both atmospheric and oceanic parameters into genesis diagnostics for a region like BoB which experiences more cyclones over the NIO.

Despite strong evidence linking ocean conditions to cyclone genesis and intensification (Shay et al., 2000; Wu et al., 2007; Lin et al., 2009; Goni and Trinanes, 2009; Naresh Krishna et al., 2013; Zhang et al., 2016; Ditchek et al., 2016) many GPI formulations lack oceanic components. Recent studies have emphasized the importance of ocean-atmosphere interaction. Mall et al. (2019) analyzed the spatial and temporal variability of cyclone genesis over the BoB and reported that variations in large-scale ocean-atmosphere interactions, including SST and vertical wind shear, play a crucial role in modulating cyclone formation particularly in the post-monsoon season. In addition, Shay et al. (2011) highlighted the role of upper ocean thermal structure such as SST fronts and sea surface height anomalies (SSHAs) in the formation of Cyclone Nargis, demonstrating that ocean subsurface conditions can significantly influence the genesis and intensification of tropical cyclones (TCs).

Tropical cyclone genesis forecasting is essential for disaster preparedness and mitigation, particularly for coastal regions prone to extreme weather events. Traditional GPIs have primarily relied on atmospheric parameters to estimate the potential for cyclone formation. Building on this foundation, Suneeta and Sadhuram (2018) advanced the GPI framework by incorporating oceanic variables, notably UOHC (kJ/cm^{-2}), alongside key atmospheric factors. This integration improved the representation of ocean-atmosphere interactions influencing cyclone development. Suneeta and Ramakrishna (2021) further extended the framework by introducing SSH (m) into the GPI formulation for the first time in the (BoB) context. This enhancement strengthened the index's ability to capture upper-ocean thermal variability, a critical factor in cyclone formation and intensification. The modified indices demonstrated strong correlations with cyclone activity during the peak and post-monsoon seasons ($r = 0.80$ to 0.83), all statistically significant at the 99 % confidence level.

The present study differs substantially in both scope and methodology. In our earlier work, the relationship between GPIs and the Total Number of Depressions and Cyclones (TNDC) was explored in a broader statistical context without cyclone-specific analysis. By contrast, the current study applies the newly developed GPI formulations to detailed case studies of multiple post-monsoon cyclones over the BoB. Specifically, we evaluate three distinct indices: (i) GPIK, the original atmospheric-only index developed by Kotal et al. (2009); (ii) GPIS, which incorporates UOHC as introduced by Suneeta and Sadhuram (2018); and (iii) GPIS1, which includes a squared SSH term to capture nonlinear oceanic effects, as proposed by Suneeta and Ramakrishna (2021). For clarity, the term "GPIs" in this study collectively refers to these three indices and does not imply any combination of GPIS and GPIS1.

Our work extends earlier research by systematically comparing the performance of these indices for multiple post-monsoon cyclones over the BoB using high-resolution datasets, including ERA5 hourly reanalysis and 0.25° AVISO/CMEMS ocean data. We demonstrate that GPIS1, which includes both UOHC and SSH, improves cyclone genesis prediction lead time to 3–4 days significantly longer than the 1-day lead time provided by the operational atmospheric GPI used by the IMD. By integrating atmospheric and oceanic variables within a multi-index framework, this study offers a more comprehensive and operationally relevant approach to cyclone genesis forecasting during the BoB post-monsoon season. This improvement is crucial for enhancing early warning systems, enabling better mitigation planning and building resilience in vulnerable coastal communities.

2. Data and methodology

The present study employed three distinct GPIs for forecasting tropical cyclone genesis over the BoB during the post-monsoon season. The first GPI, referred to as GPIK is calculated following the methodology proposed by Kotal et al. (2009) and is denoted as GPIK ('K' for Kotal) in this study to clearly identify it as the version based solely on atmospheric parameters. This index corresponds to the one currently used

operationally by the India Meteorological Department (IMD). The GPIK is computed using the following equation 1:

$$\mathbf{GPIK} = \frac{\xi_{850} \times M \times I}{S} \text{ if } \xi_{850} > 0, M > 0 \text{and } I > 0 \rightarrow = 0 \text{ if } \xi_{850} \leq 0, M \leq 0 \text{ or } I \leq 0 \quad (1)$$

where

ξ_{850} = low -level relative vorticity (at 850 hPa) in (10^{-5} S^{-1}),

S= Vertical wind shear between 200 hPa and 850 hPa (m S^{-1}),

$M = \frac{[RH-40]}{30}$ = Middle troposphere relative humidity; RH is the average relative humidity between 700 hPa and 500 hPa (%),

I= (T850-T500) ^{0}C = Middle tropospheric instability (Temperature difference between 850 hPa and 500 hPa) (°C).

The second GPI, referred to as GPIS ('S' for Sadhuram and Suneeta), was proposed in an earlier study by Suneeta and Sadhuram (2018) and modifies GPIK through the inclusion of the upper ocean thermal structure via the UOHC, such that the formulation becomes:

$$\mathbf{GPIS} = \mathbf{GPIK} * \left(\frac{UOHC}{40}\right) \quad (2)$$

UOHC (kJ/cm^2) in equation (2) is calculated using the multiple regression equation proposed by Ali et al. (2012) as given in Equation (2.1)

$$\mathbf{UOHC} = -245.256 + \mathbf{D26}*0.982 + \mathbf{SSHA}*1.243 + \mathbf{SST}*8.417 \quad (2.1)$$

where

D26 is the depth (m) of the 26 °C isotherm,

SST is the Sea Surface Temperature (°C),

SSHA is the Sea Surface Height Anomaly (m).

The D26 parameter is estimated using the regression relationship of Sadhuram et al. (2006) as follows in equation (2.2).

$$D26 = 63.84 + 1.39*SSHA + 0.044SSHA*SSHA \quad (2.2)$$

D26 was estimated using the empirical relationship proposed by Sadhuram et al. (2006) which demonstrated a strong correlation ($r = 0.76$) between D26 and SSHA. Equation (2.2) defines D26 as a function of both SSHA and SST (°C).

The third GPI, referred to as GPIS1 ('S' for Suneeta and SSVS Ramakrishna), was refined by Suneeta and Ramakrishna (2021) and further modifies GPIS through the inclusion of SSH, such that the formulation becomes:

$$\mathbf{GPIS1} = \mathbf{GPIS}\ X\ (\mathbf{SSH}*\mathbf{SSH}) \quad (3)$$

In this formulation, SSH is squared to enhance the sensitivity of the index to variations in upper ocean dynamic height, which is often associated with increased oceanic heat content key factor influencing cyclone intensification. The use of the squared term was empirically derived from correlation analysis, which revealed that the nonlinear relationship between SSH and cyclone genesis potential was better captured by squaring SSH. This modification improved the skill of the index in identifying favorable cyclogenesis environments.

Atmospheric variables for computing GPIK were extracted from the ERA5 reanalysis dataset produced by the European Centre for Medium-Range Weather Forecasts (ECMWF), with a horizontal resolution of ~0.25° (~31 km) hourly temporal resolution and multiple vertical levels. For oceanic parameters, SST and SSHA were obtained from the AVISO datasets distributed via the Copernicus Marine Environment Monitoring Service (CMEMS) at 0.25° × 0.25° resolution. Unlike earlier works that utilized coarser-resolution atmospheric inputs (2.5° × 2.5°), the present analysis employs high-resolution atmospheric and oceanographic data to improve the accuracy and consistency of GPI computations.

The analysis focused on severe to very severe cyclones that occurred over the BoB between 2016 and 2022. Four post-monsoon tropical cyclones were examined: *Kyant* (2016), *Bulbul* (2019), *Burevi* (2020), and *Mandous* (2022). These cases were selected for their diverse synoptic features, tracks and intensities enabling a comprehensive evaluation of the GPIs under varied environmental conditions. Each cyclone was analyzed from its genesis date back to five days prior defined as the spin-up period to assess the ability of the GPIs to capture pre-genesis environmental signals. For instance, Cyclone *Kyant* which formed as a deep depression on 21 October 2016 was tracked from 16 to 21 October. Cyclone *Bulbul* a very severe cyclonic storm was analyzed from 1 to 5 November 2019; Cyclone *Burevi* from 25 to 30 November 2020; and Cyclone *Mandous* from 21 to 26 December 2022. Using consistent five-day spin-up periods ensured comparability in evaluating the predictive performance of the different GPI formulations. To assess predictive skill, the Pearson correlation coefficient (r) and RMSE were calculated between the index values and observed cyclone genesis occurrences. These statistics were computed for both spin-up and genesis periods. A summary of each cyclone's genesis date, track, intensity, landfall characteristics and spin-up period is provided in Table 1, supporting the analysis of synoptic variability and GPI responsiveness across events.

2.1. Basic information on cyclogenesis

To demonstrate the proposed GPIs four notable tropical cyclones that occurred between 2016 and 2022 over the BoB were selected as case studies. Cyclone *Kyant*, considered as Case Study 1, originated as a deep depression over the BoB and intensified into a cyclonic storm on October 21, 2016 with maximum sustained winds of approximately 65 km/h and a central pressure near 1000 hPa. It remained relatively weak and did not evolve into a severe cyclone gradually weakening by October 27 without making significant landfall. Case Study 2, Cyclone *Bulbul* developed in early November 2019 and intensified into a severe cyclonic storm reaching peak winds of 115 knots (213 km/h) with a minimum central pressure of 970 hPa. It made landfall near the West Bengal Bangladesh border on November 9 with slightly reduced intensity (70–75 knots) causing widespread impact. Cyclone *Burevi* the focus of Case Study 3 formed in early December 2020 and made landfall on Sri Lanka's northeastern coast

Table 1
Year wise Cyclones information

Year	Cyclone Name	Genesis Date	Genesis Period	Maximum Intensity (kt)	Coast of Landfall
2016	***Kyant***	21/10/2016	16/10/2016 to 21/10/2016	45 (kt)	Andaman Islands, Myanmar, South India
2019	***Bulbul***	05/11/2019	01/11/2019 to 05/11/2019	115 (kt)	Sundarbans region border of West Bengal, India, and southwestern Bangladesh
2020	***Burevi***	30/11/2020	25/11/2020 to 30/11/2020	55 (kt)	Sri Lanka, Tamil Nadu, Kerala
2022	***Mandous***	26/12/2022	21/12/2022 to 26/12/2022	45 (kt)	Tamil Nadu, Andhra Pradesh, Sri Lanka

near Trincomalee on December 2 with sustained winds of about 75 km/h. It triggered heavy rainfall and flooding leading to the evacuation of over 75,000 people. After crossing Sri Lanka, it entered the Gulf of Mannar and weakened into a deep depression bringing moderate rainfall and gusty winds to southern Tamil Nadu and Kerala. Case Study 4, Cyclone *Mandous* formed in December 2022 and intensified into a cyclonic storm over the BoB, making landfall near Chennai on December 9 with peak winds around 45 knots (85 km/h). It caused heavy rainfall, strong winds, uprooted trees, widespread power outages and significant disruptions across Tamil Nadu and parts of Andhra Pradesh particularly affecting agriculture and local infrastructure.

3. Results and discussion

3.1. Case study 1

The genesis period for Cyclone *Kyant* was identified as 16–21 October 2016. Daily GPIK distributions for this period computed using atmospheric parameters in accordance with Equation (1), are shown in Figure 1(a). The results reveal clear signals of cyclogenesis two days prior to the event particularly on 19–20 October, with the black dot indicating the genesis location and the dotted line depicting the cyclone track. Figure 1(b) and (c) illustrate that GPIS and GPIS1 derived from Equations (2) and (3) and incorporating both atmospheric and oceanic parameters provided earlier and stronger indications of cyclogenesis compared to GPIK. Along the cyclone track elevated GPI values were observed with an overall range of 0–30 signifying favorable conditions for cyclone development. Figure 2(a-d) presents the mean spatial distributions of individual oceanic parameters during the genesis period. SST values (Figure 2(a)) ranged from 27 °C to 31 °C with temperatures exceeding 28 °C along the cyclone track, indicating thermally favorable conditions for cyclogenesis. SSH (Figure 2(b)) varied between 0.2 and 0.8 m, while UOHC values ranged from 50 to 200 (kJ/cm^2) with values above 150 (kJ/cm^2) observed along the track and at the genesis location. As noted in previous studies (Maneesha, 2013; Suneeta & Sadhuram, 2018) such elevated UOHC values are conducive to tropical cyclone development. D26 depths (Figure 2(d)) ranged from 50 to 175 m near the genesis region and along the track with higher values indicating enhanced subsurface heat content supportive of cyclogenesis.

During this period, the highest correlation ($r = 0.74$) was observed between GPIK and GPIS1, accompanied by the lowest RMSE (3.22) indicating the strongest agreement in representing environmental conditions favorable for cyclogenesis. In contrast, the correlation between GPIK and GPIS was relatively low ($r = 0.44$, RMSE = 4.50) while GPIS and GPIS1 showed moderate correspondence ($r = 0.53$, RMSE = 3.92). Although the correlation values among all index pairs were not uniformly high (Table 2), GPIS1 demonstrated the greatest overall consistency particularly in its alignment with GPIK. These findings emphasize the critical role of oceanic parameters especially SST, SSH, UOHC and D26 in modulating cyclone genesis during the five-day spin-up phase preceding the event.

3.2. Case study 2

For Cyclone *Bulbul* Figure 3(a) displays GPIK values ranging from 0 to 30 with higher values concentrated near the cyclone track indicating favorable conditions for genesis. The black dot marks the genesis location, while the dotted line denotes the cyclone track. GPIK signalled the potential for cyclogenesis approximately two days in advance specifically from 3 to 4 November 2019. In contrast Figure 3(b) and (c) show that GPIS and GPIS1 which incorporate oceanic parameters provided clearer indications of cyclogenesis 4–5 days prior to the event. Among these GPIS1 exhibited the most pronounced signal suggesting that indices integrating oceanic variables outperform GPIK based solely on atmospheric parameters in identifying early cyclone formation signals. Figure 4(a-d) presents the average spatial distributions of key oceanic parameters SST, D26, UOHC and SSH during the genesis period. SST ranged between 27 °C and 31 °C, SSH varied from 0.5 to 2.0 m, UOHC ranged from 25 to 200 kJ/cm^{-2} and D26 extended from 60 to 160 m. Elevated values of these parameters were observed in proximity to the cyclone track reflecting thermodynamically favorable conditions for cyclogenesis. These spatial patterns corroborate previous studies linking higher SST, deeper D26 greater UOHC and increased SSH with enhanced tropical cyclone development potential.

During Cyclone *Bulbul's* genesis period, strong interrelationships were observed among all GPI indices. The highest correlation ($r = 0.94$) was recorded between GPIS and GPIS1, as well as between GPIK and GPIS, indicating substantial coherence among the indices. The lowest RMSE

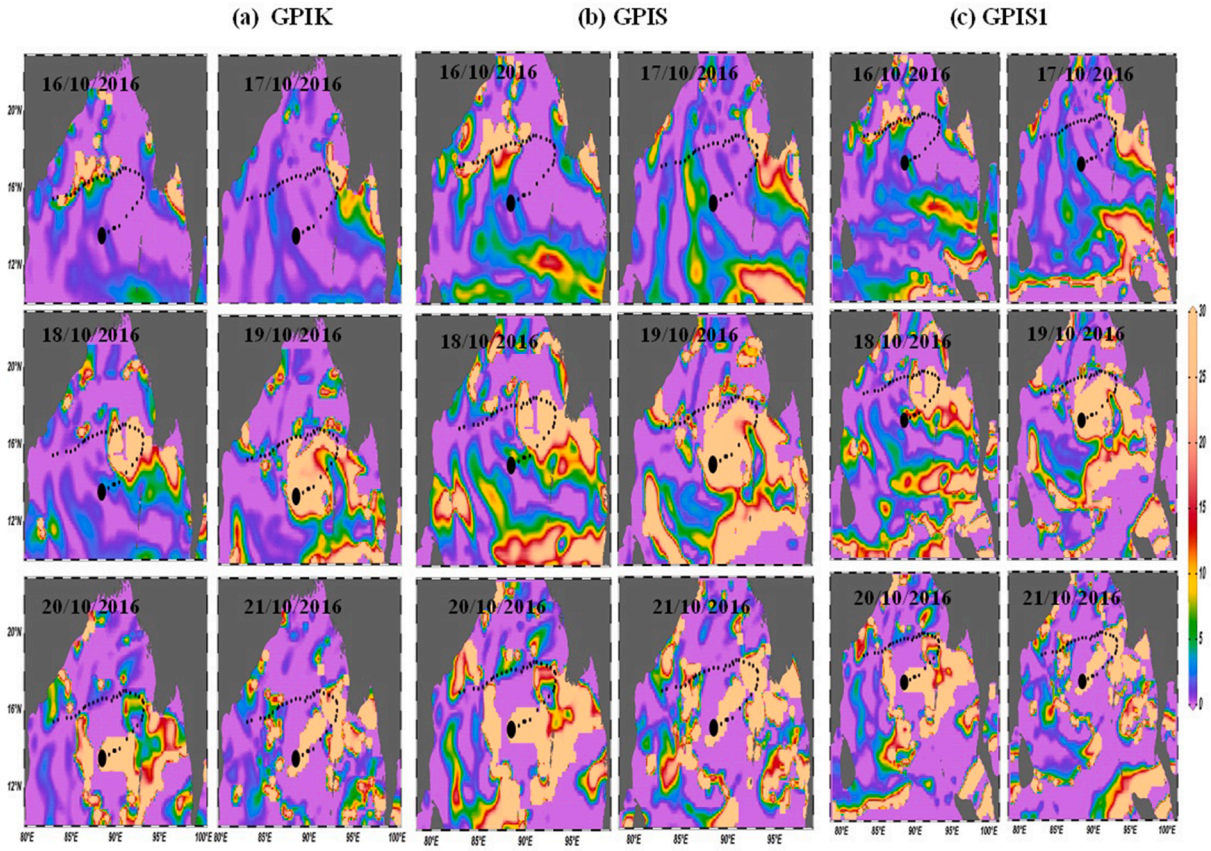

Figure 1. **(a-c):** Daily spatial distributions during cyclone *Kyant* from the period 16th to 21st October 2016. Black dot indicates the genesis location dotted line indicates the track of the cyclone. (a) GPIK, (b) GPIS and (c) GPIS1 over BoB.

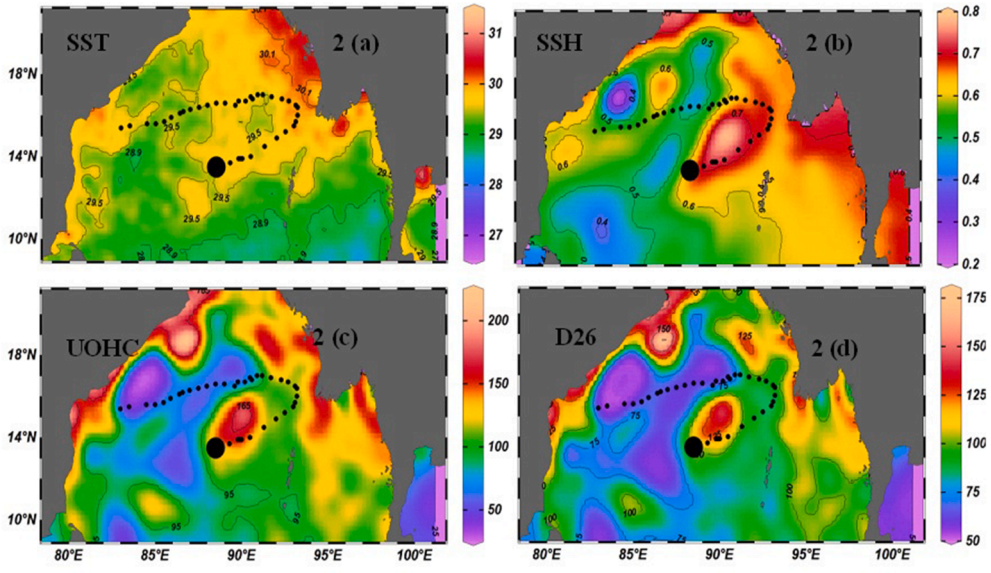

Figure 2. **(a-d):** Individual parameters average from 16th to 21st October 2016 in *Kyant* cyclone period.

(2.44) was found between GPIK and GPIS followed by 3.85 between GPIS and GPIS1 (Table 3). These results highlight strong internal consistency within the indices with the GPIS and GPIS1 combination being particularly effective in delineating cyclogenesis potential. Overall, this analysis underscores the critical importance of incorporating oceanic parameters to enhance the accuracy and lead time of tropical cyclone genesis forecasts.

Table 2
GPIs Correlation and RMSE during *Kyant* cyclone period.

GPIs for *KYANT* Cyclone	GPIK	GPIS	GPIS1
GPIK	Corr: **1.00** RMSE: **0.00**	Corr: **0.44** RMSE: **4.50**	Corr: **0.74** RMSE: **3.22**
GPIS	Corr: **0.44** RMSE: **4.50**	Corr: **1.00** RMSE: **0.00**	Corr: **0.53** RMSE: **3.92**
GPIS1	Corr: **0.74** RMSE: **3.22**	Corr: **0.53** RMSE: **3.92**	Corr: **1.00** RMSE: **0.00**

3.3. Case study 3

Figure 5(a) illustrates the genesis of Cyclone *Burevi* on 30 November 2020. The GPIK index provided an initial indication of cyclogenesis on 25 November; however, no significant signals were detected on 26–27 November. A weak signal re-emerged on 28 November but a clear indication from GPIK was evident only two days prior to the actual genesis. In contrast, Figure 5(b) and (c) presenting GPIS and GPIS1 computed using Equations (2) and (3) respectively exhibit clearer and more consistent cyclogenesis signals from 25 to 30 November, particularly near the cyclone's genesis location. These observations suggest that GPIS and GPIS1 outperformed GPIK in capturing early cyclone formation signals for this event. Figure 6(a-d) displays the spatial distributions of key oceanic parameters SST, SSH, D26, and UOHC during the genesis period. SST ranged from 26 °C to 29.5 °C, SSH from 0.5 to 2.5 m, D26 from 65 to 82.5 m and UOHC from 50 to 90 kJ/cm^{-2} with preeminent values observed near the genesis location and along the cyclone track. These parameters indicate thermodynamically favorable conditions for cyclone development.

Statistical analysis of Cyclone *Burevi* revealed strong consistency across all GPI formulations. The highest correlation ($r = 0.94$) and lowest RMSE (2.36) were observed between GPIK and GPIS1 as detailed in Table 4. An even stronger correlation ($r = 0.96$) was found between GPIS and GPIS1 demonstrating a close relationship between these indices. These findings reinforce the robustness of GPIS1 which exhibited reliable and consistent performance in this case counter to earlier assumptions of its limited skill. This analysis underscores the strong agreement between the newly developed indices and observed cyclone development with elevated oceanic parameters supporting favorable conditions for cyclogenesis along *Burevi's* track.

3.4. Case study 4

In Figure 7(a) the genesis location of Cyclone *Mandous* is indicated by a dotted circle while its track is represented by a dotted line. The GPIK index exhibited spatial variations from 21 to 26 December with cyclogenesis occurring on 26 December. However, during the five days preceding the event (21–25 December), GPIK provided only limited indications of impending cyclogenesis. In contrast, Figure 7(b) and (c) depicting GPIS and GPIS1 respectively show considerably stronger signals of cyclogenesis along the cyclone track with elevated GPI values concentrated near the genesis location. These indices integrating both atmospheric and oceanic parameters were more effective in capturing pre-genesis environmental conditions. Figure 8(a-d) presents the average spatial distributions of key oceanic parameters during Cyclone *Mandous'* genesis period. UOHC ranged from 50 to 250 kJ/cm^{-2} (Figure 8(a)) while D26 values varied between 50 and 175 m (Figure 8(b)). SST fluctuated between 20 °C and 30 °C

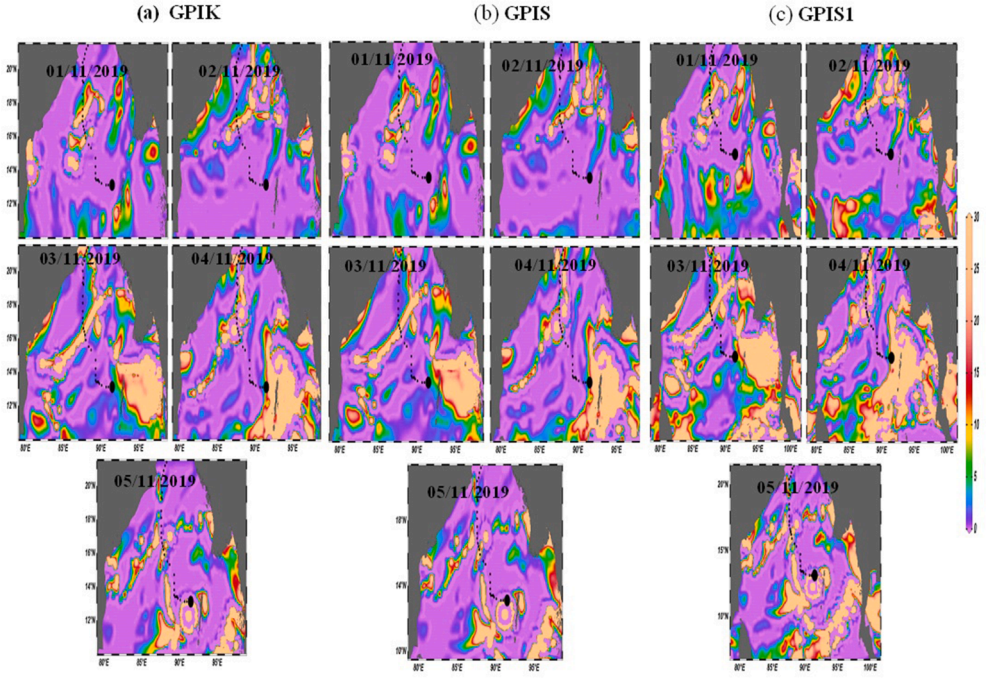

Figure 3. **(a-c):** Daily spatial distributions during cyclone *Bulbul* from the period 1st to 5th November 2019.

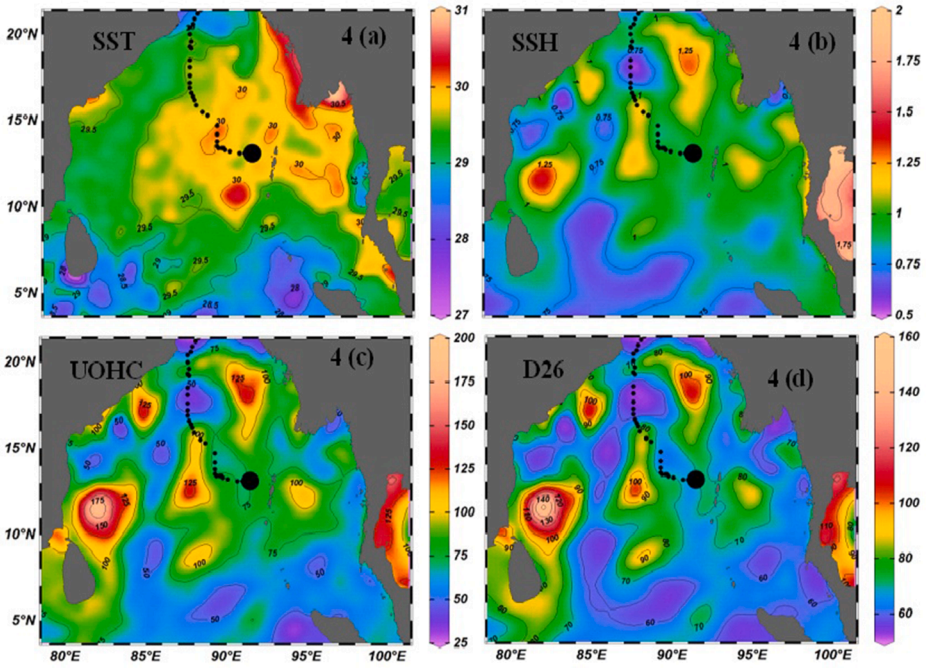

Figure 4. **(a-d):** Individual parameters averages from 1st to 5th November 2019 in *Bulbul* cyclone period.

Table 3
GPIs Correlation and RMSE during *Bulbul* cyclone period.

GPIs for *BULBUL* Cyclone	GPIK	GPIS	GPIS1
GPIK	Corr: **1.00** RMSE: **0.00**	Corr: **0.94** RMSE: **2.44**	Corr: **0.91** RMSE: **4.26**
GPIS	Corr: **0.94** RMSE: **2.44**	Corr: **1.00** RMSE: **0.00**	Corr: **0.94** RMSE: **3.85**
GPIS1	Corr: **0.91** RMSE: **4.26**	Corr: **0.94** RMSE: **3.85**	Corr: **1.00** RMSE: **0.00**

(Figure 8(c)) and SSH ranged from 0.6 to 1.6 m (Figure 8(d)). Notably elevated UOHC, D26 and SST values were observed along the cyclone track during the genesis phase indicating favorable thermodynamic conditions for cyclone development.

Statistical analysis revealed a strong correlation ($r = 0.96$) between GPIK and GPIS1 accompanied by the lowest RMSE value of 1.79, reflecting a high degree of agreement between these indices. The GPIK and GPIS pair also exhibited a good correlation ($r = 0.88$) albeit with a higher RMSE of 4.68. Despite variability in RMSE values GPIS1 maintained consistent agreement with GPIK underscoring its reliability and robustness in representing cyclone genesis potential (Table 5).

Figure 9(a-d) presents bar charts illustrating the mean daily values of three Genesis Potential Indices GPIK, GPIS, and GPIS1 during the five-day period preceding the genesis of four cyclones: *Kyant, Bulbul, Burevi*, and *Mandous*. The x-axis denotes the number of days prior to genesis (Day −5 to Day 0) while the y-axis represents the corresponding mean GPI values. Blue bars correspond to GPIK, with orange and green bars representing GPIS and GPIS1 respectively. Figure 9(a) pertains to Cyclone *Kyant* (16–21 October 2016), Figure 9(b) to *Bulbul* (1–5 November 2019), Figure 9(c) to *Burevi* (25–30 November 2020) and Figure 9(d) to *Mandous* (21–26 December 2022). Across all four cyclones GPIS and GPIS1 consistently exhibit higher mean values than GPIK on most days leading up to genesis. This pattern suggests that the modified indices which incorporate both atmospheric and oceanic parameters provide a more robust indication of favorable pre-genesis conditions than GPIK which relies solely on atmospheric variables. Furthermore, GPIK generally displays lower and more variable values indicating reduced sensitivity or predictability in capturing cyclogenesis potential under certain conditions. In contrast, GPIS and GPIS1 demonstrate more stable and consistent patterns across the cases reinforcing their effectiveness in identifying environments conducive to cyclone formation.

Figure 10(a-d) presents heat maps illustrating the correlation matrices among the three Genesis Potential Indices GPIK, GPIS, and GPIS1 for four cyclones: *Kyant, Bulbul, Burevi*, and *Mandous*. These visualizations and accompanying statistics provide insight into the consistency and reliability of the indices across diverse cyclonic environments. In Figure 10(a) (Cyclone *Kyant*) GPIK and GPIS1 exhibit a strong correlation ($r = 0.74$, RMSE = 3.22) whereas GPIK and GPIS show a lower correlation ($r = 0.44$, RMSE = 4.50) indicating that GPIS1 aligns more closely with the traditional GPIK. The moderate agreement between GPIS and GPIS1 ($r = 0.53$, RMSE = 3.92) highlights the added value of oceanic parameters in GPIS1 for capturing genesis potential. Figure 10(b) (Cyclone *Bulbul*) reveals an exceptionally high correlation between GPIS and GPIS1 ($r = 0.99$, RMSE = 0.42), confirming their tight coupling. GPIK shows slightly lower

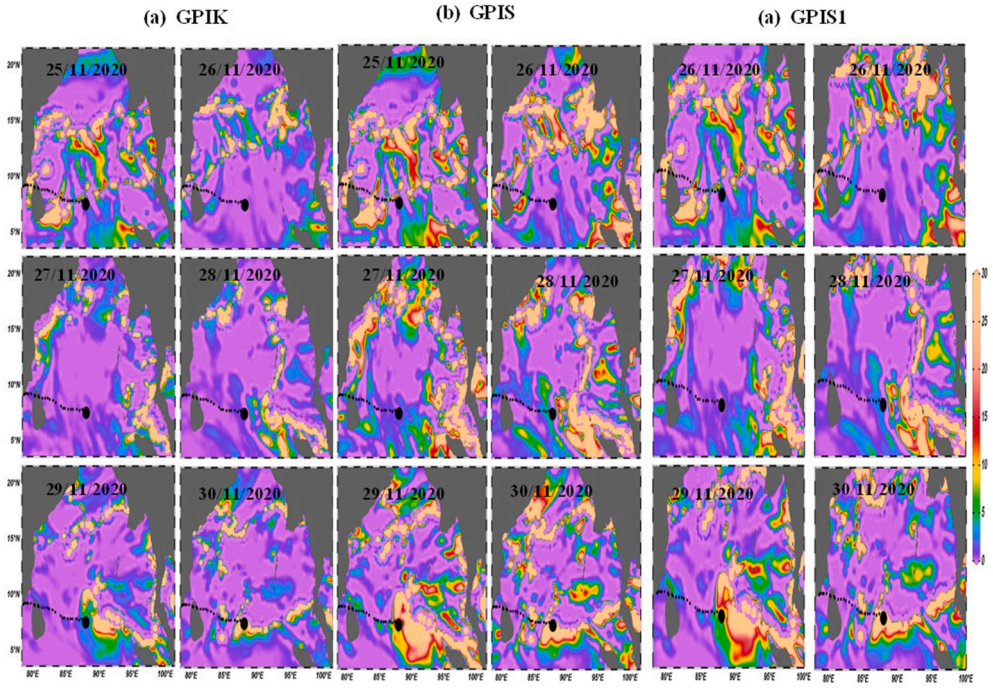

Figure 5. **(a-c):** Daily spatial distributions during cyclone *Bruvi* from the period 25th to 30th November 2020.

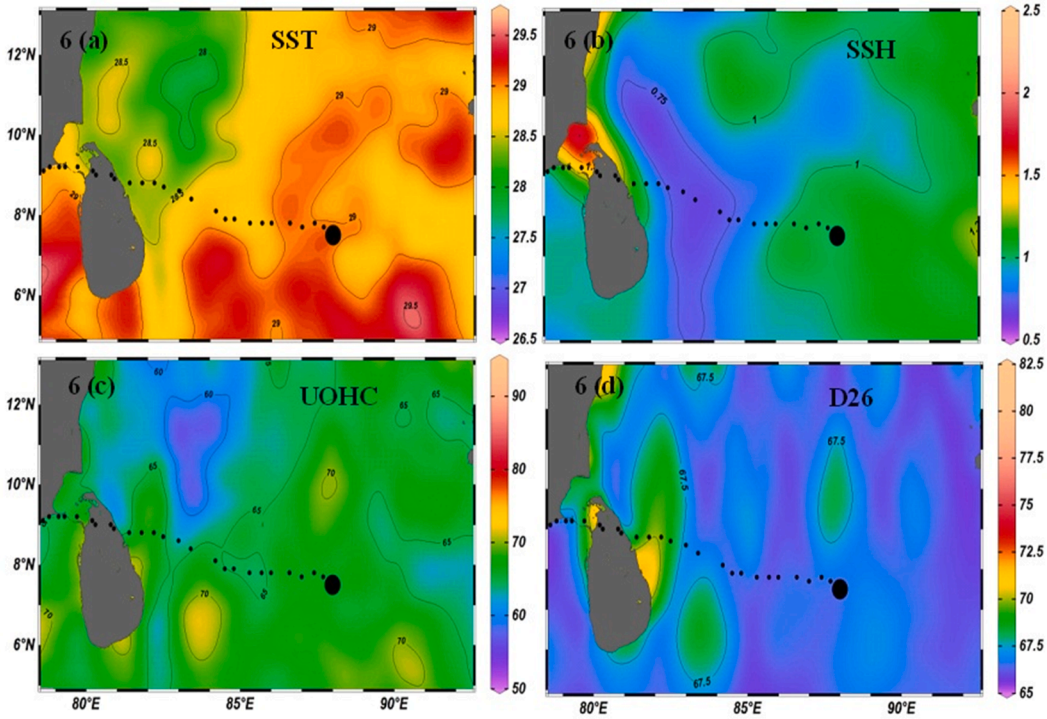

Figure 6. **(a-d)**: Individual parameters averages from 25th to 30th November 2020 in cyclone *Bruvi.*

correlations with GPIS ($r = 0.87$, RMSE = 5.14) and GPIS1 ($r = 0.88$, RMSE = 4.72) indicating moderate-to-strong agreement and underscoring the sensitivity of the modified indices to coupled ocean-atmosphere conditions. In Figure 10 (c) (Cyclone *Burevi*) all three GPIs demonstrate strong positive correlations. The highest agreement is observed between GPIS and GPIS1 ($r = 0.96$, RMSE = 2.31) followed closely by GPIK and GPIS1 ($r = 0.94$, RMSE = 2.36) and GPIK and GPIS ($r = 0.93$, RMSE = 3.45). These results indicate a high degree of consistency among the indices during Cyclone *Burevi's* genesis phase demonstrating that both the original and modified GPIs effectively captured the environmental

Table 4
GPIs Correlation and RMSE during *Bruvi* cyclone period.

GPIs for *BRUVI* Cyclone	GPIK	GPIS	GPIS1
GPIK	Corr: **1.00** RMSE: **0.00**	Corr: **0.93** RMSE: **3.45**	Corr: **0.94** RMSE: **2.36**
GPIS	Corr: **0.93** RMSE: **3.45**	Corr: **1.00** RMSE: **0.00**	Corr: **0.96** RMSE: **2.31**
GPIS1	Corr: **0.94** RMSE: **2.36**	Corr: **0.96** RMSE: **2.31**	Corr: **1.00** RMSE: **0.00**

Table 5
GPIs Correlation and RMSE during *Mandous* cyclone period.

GPIs for *MANDOUS* Cyclone	GPIK	GPIS	GPIS1
GPIK	Corr: **1.00** RMSE: **0.00**	Corr: **0.88** RMSE: **4.68**	Corr: **0.96** RMSE: **1.79**
GPIS	Corr: **0.88** RMSE: **4.68**	Corr: **1.00** RMSE: **0.00**	Corr: **0.91** RMSE: **4.14**
GPIS1	Corr: **0.96** RMSE: **1.79**	Corr: **0.91** RMSE: **4.14**	Corr: **1.00** RMSE: **0.00**

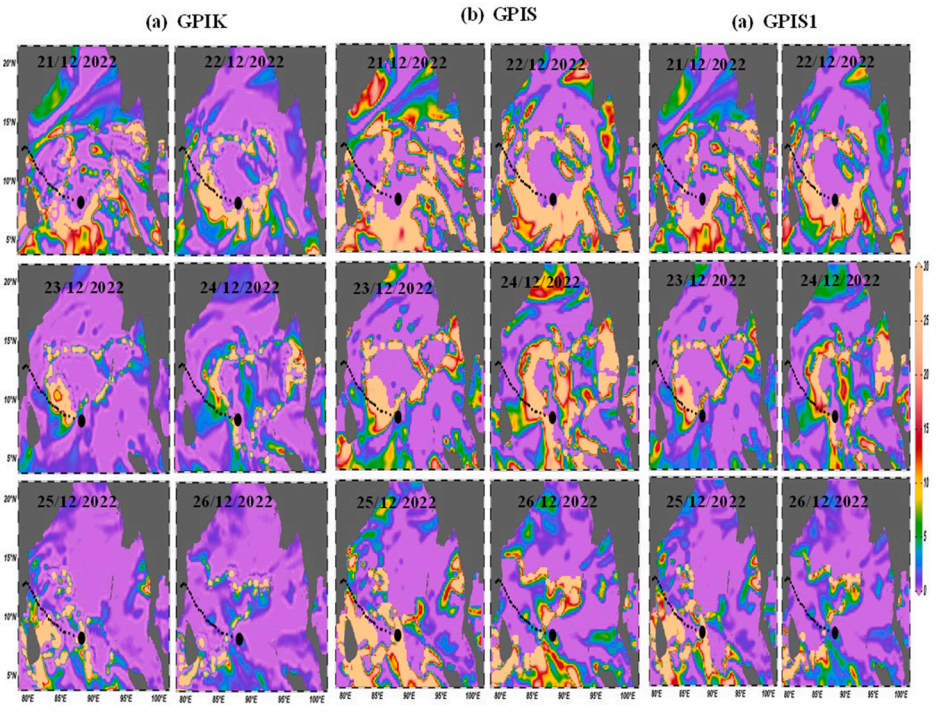

Figure 7. **(a-c):** Daily spatial distributions during cyclone *Mandous* from the period 21st to 26th December 2022.

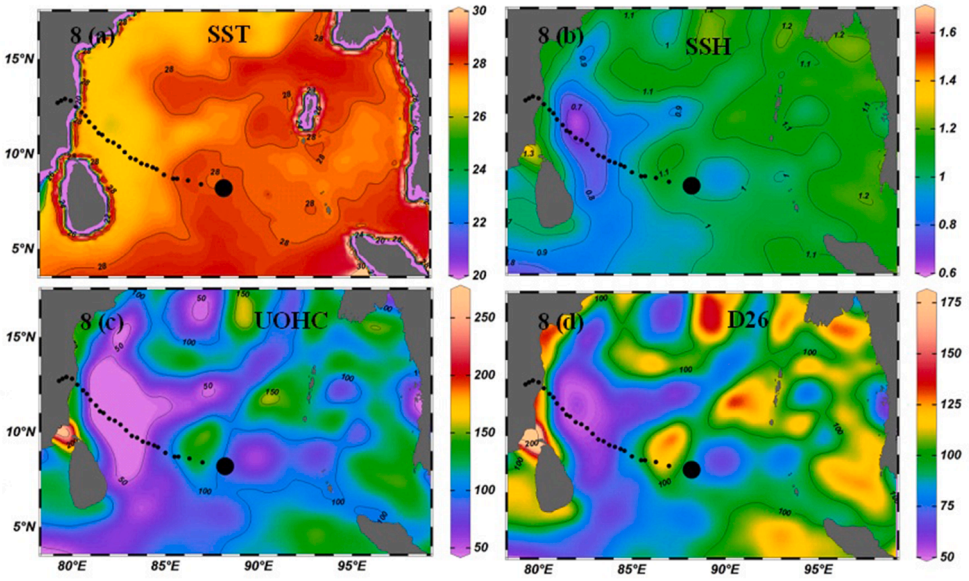

Figure 8. **(a-d):** Individual parameters averages from 21st to 26th December 2022 in cyclone *Mandous*.

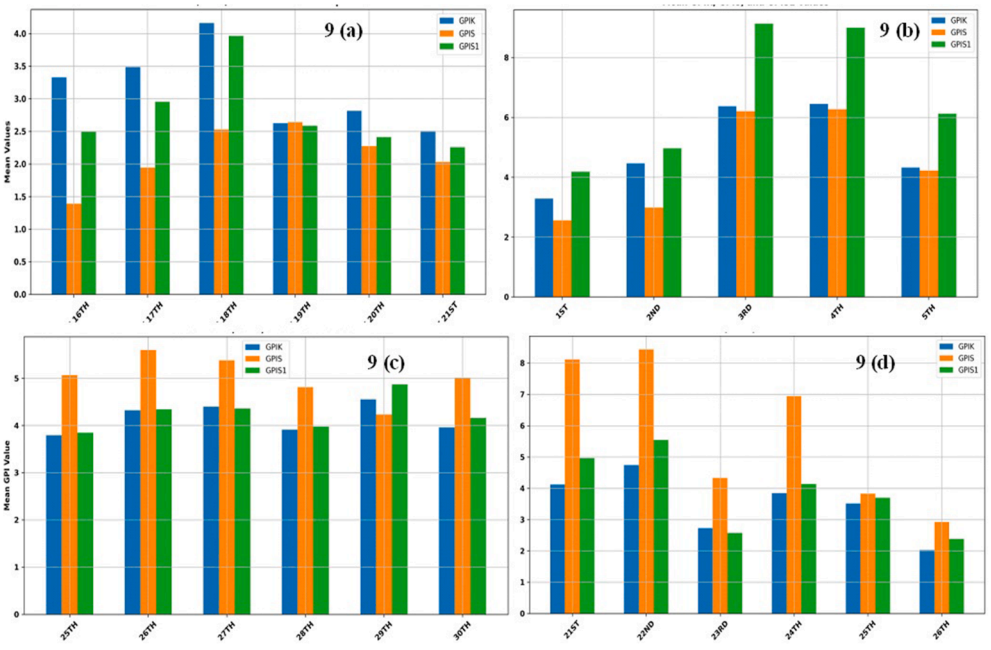

Figure 9. **(a-d):** Mean values bar diagram for *Kyant, Bulbul, Bruvi* and *Mandous* cyclones period.

Figure 10. **(a-d):** Correlation Heat Maps of GPIK, GPIS, and GPIS1 Indices for *Kyant*, *Bulbul*, *Bruvi*, and *Mandous* Cyclones.

conditions favorable for cyclogenesis despite complex environmental variability. Figure 10(d) (Cyclone *Mandous*) again shows the highest correlation between GPIK and GPIS1 ($r = 0.96$, RMSE $= 1.79$). GPIS and GPIS1 are also strongly correlated ($r = 0.91$, RMSE $= 4.14$), while GPIK and GPIS show slightly lower alignment ($r = 0.88$, RMSE $= 4.68$). This pattern further supports GPIS1's consistent agreement with both GPIK and GPIS, reinforcing its reliability across diverse cyclonic scenarios. Overall, the correlation and RMSE analyses across all four cyclones confirm that GPIS1 not only

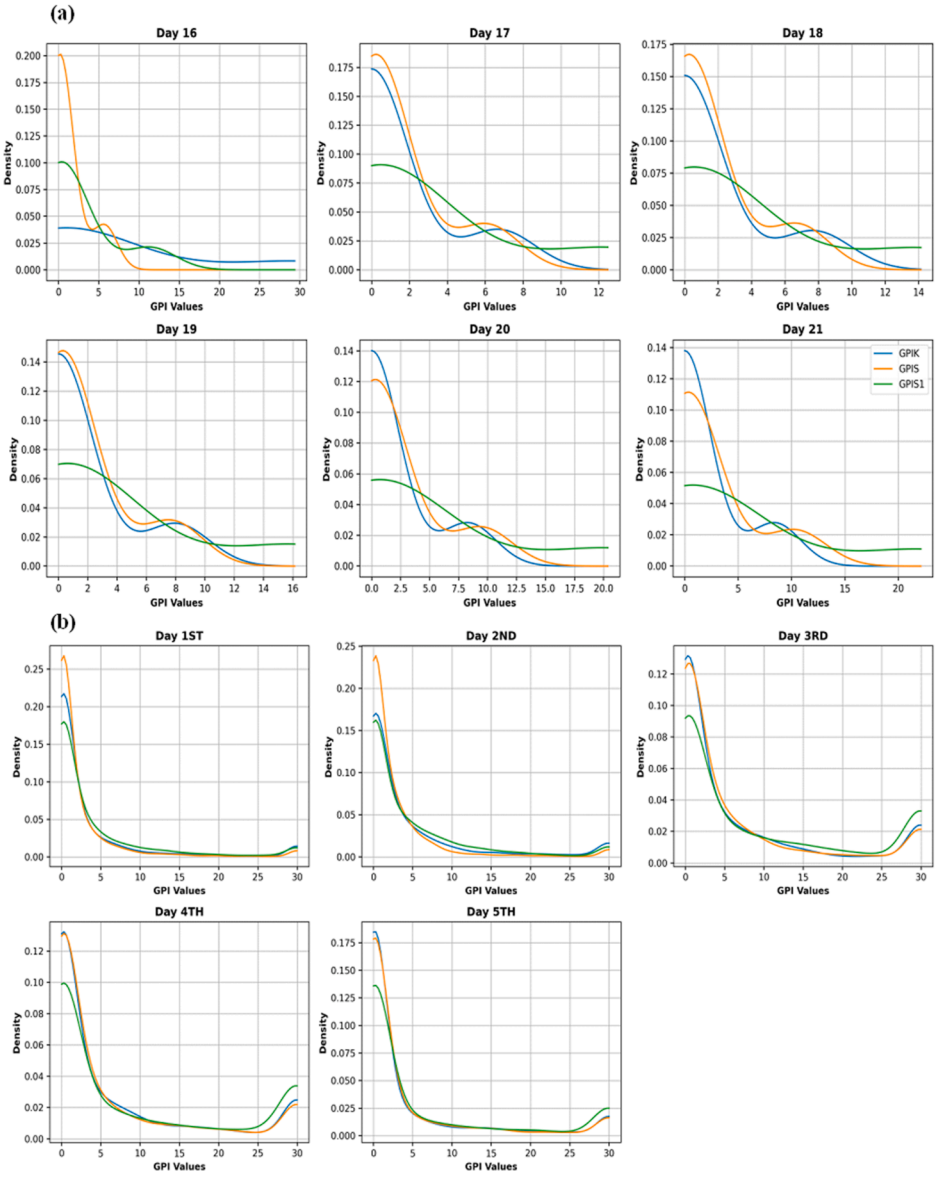

Figure 11. **(a-b)**: Probability density distributions for the different cyclone indices during *Kyant* and *Bulbul* Cyclone time.

complements the traditional GPIK but also demonstrates improved consistency particularly when both atmospheric and oceanic conditions jointly influence cyclone genesis.

Figures 11(a-b) and 12(a-b) present the probability density distributions of GPI values for four cyclones *Kyant, Bulbul*, *Burevi*, and *Mandous* across multiple days leading up to their genesis. Each row corresponds to a specific day within the genesis period, with the probability density of each cyclone plotted over the respective days. Different colors represent the three indices: GPIK (blue), GPIS (orange) and GPIS1 (green). Across all four cyclones GPIK distributions consistently exhibit broader and less sharply defined peaks compared to GPIS and GPIS1. For Cyclone *Kyant*, GPIS and GPIS1 display sharper and more distinct peaks on 18 and 19 October closely aligning with the actual genesis timeline whereas GPIK exhibits a wider, less concentrated distribution (Figure 11(a)). During Cyclone *Bulbul's* genesis period (1–5 November) GPIS and GPIS1 again demonstrate higher and more focused peaks particularly on Days 2 and 3 indicating a clearer representation of environmental conditions favorable for cyclone development (Figure 11(b)). Similarly, for Cyclone *Burevi* (25–30 November) GPIS and GPIS1 present more pronounced and concentrated peaks than GPIK effectively capturing the window of favorable genesis conditions (Figure 12(a)). For Cyclone *Mandous* (21–26 December) GPIS and GPIS1 consistently exhibit higher probability densities throughout the period reflecting stronger alignment with the cyclogenesis window compared to GPIK (Figure 12(b)).

The consistently sharper and more focused peaks of GPIS and GPIS1 across all cyclones imply that these modified indices more effectively isolate periods of high genesis potential. In contrast, the broader and lower peaks of GPIK indicate reduced sensitivity to key environmental factors limiting its predictive precision. These findings are consistent

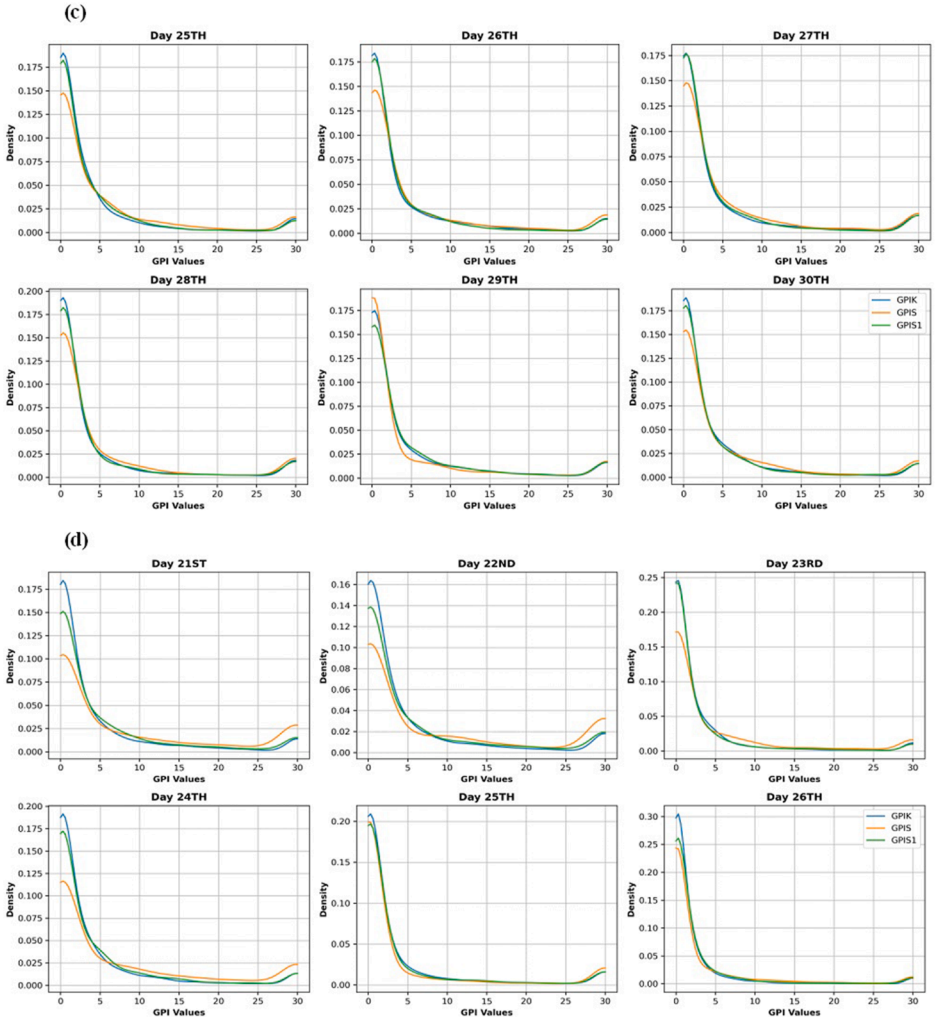

Figure 12. **(c-d)**: Probability density distributions for the different cyclone indices during *Bruvi and Mandous* Cyclone time.

with previous studies: Ghetye and Nayak (2020) found that GPIS slightly outperformed GPIK across 92 developing and 93 non-developing systems in the northern Indian Ocean, while Singh et al. (2020) demonstrated that GPIS could identify developing low-pressure systems 3–4 days in advance compared to a 1-day lead time using GPIK. Overall, these results indicate that GPIS and GPIS1 provide improved accuracy and reliability in identifying favorable conditions for cyclone genesis. The enhanced performance likely arises from the inclusion of additional oceanic and atmospheric parameters in these indices enabling a more precise characterization of the cyclogenesis environment.

4. Conclusions

The comprehensive analysis of Cyclones *Kyant, Bulbul, Burevi*, and *Mandous* highlights the critical importance of integrating both oceanic and atmospheric parameters to enhance tropical cyclone genesis prediction in the Bay of Bengal. The findings consistently demonstrate that the modified Genesis Potential Indices, GPIS and GPIS1 which incorporate both atmospheric and oceanic variables provide more accurate and consistent signals for cyclogenesis than the conventional GPIK which relies solely on atmospheric inputs. This improved performance arises from the ability of GPIS and GPIS1 to capture key environmental conditions strongly associated with cyclone development. In contrast, GPIK exhibited varying levels of correlation with GPIS and GPIS1 across different events: strong for Cyclone *Kyant*, moderate for *Bulbul* and *Mandous*, and lower for *Burevi*. This suggests that GPIK may lack sensitivity to crucial oceanic factors influencing cyclone genesis. The analysis further emphasizes GPIS1's robust and consistent performance particularly when paired with GPIK or GPIS. For instance, in Cyclones *Bulbul* and *Mandous*, the GPIK - GPIS1 pair yielded the highest correlations ($r = 0.96$) and the lowest RMSE values, confirming their strong agreement in representing the cyclogenesis environment. Similarly, for *Kyant*, GPIK - GPIS1 outperformed other index pairs, while for *Burevi*, all indices demonstrated strong agreement further highlighting GPIS1's reliability. These results underscore GPIS1's potential as a robust and adaptable index although its effectiveness may vary depending on storm-specific dynamics and environmental conditions highlighting the need for a multi-index adaptive GPI framework to improve cyclone prediction in the Bay of Bengal.

Correlation and RMSE analyses supported by heatmaps and probability density plots reinforce the effectiveness of GPIS and GPIS1. These indices consistently exhibited sharper distributions and higher probability density peaks indicating superior sensitivity to the atmospheric–oceanic interactions that govern cyclogenesis. In contrast, GPIK often displayed broader and flatter distributions reflecting reduced responsiveness to dynamic pre-cyclone conditions. In conclusion, the incorporation of oceanographic parameters into the GPI framework through GPIS and GPIS1 represents a significant advancement in cyclone genesis forecasting. The consistent performance of these indices across multiple cyclones underscores their superior capability in capturing favorable conditions for cyclogenesis. Adoption of GPIS and GPIS1 in operational forecasting models could markedly improve early-warning systems, enhance disaster preparedness, and strengthen risk management strategies for vulnerable coastal populations throughout the Indian Ocean region.

Author statement

P.Suneeta: Idea behind the work, Data collection for required work, overall work regarding this study and manuscript preparation: TVS Udaya Bhaskar: Supervised and contributed to formulating the underlying concept Improvement in writing quality: E Pattabi Rama Rao: Improvement in writing quality, Technical inputs in the analysis and Supervision formulation. S.S.V.S Ramakrishna: Improvement in writing quality, Technical inputs in the analysis: C.V Naidu: Suggestions for improving the manuscript to enhance its quality and impact.

Data availability

The sources for various data used in this study: SSH data from(https://data.marine.copernicus.eu/product/SEALEVEL_GLO_PHY_CLIMATE_L4_MY_008_057/download?dataset=c3s_obs-sl_glo_phy-ssh_my_twosat-l4-duacs-0.25deg_P1D_202112), IMD best track data from (https://rsmcnewdelhi.imd.gov.in/report.php?internal_menu=MzM=), ERA5 hourly data from (https://cds.climate.copernicus.eu/datasets/reanalysis-era5-pressure-levels?tab=overview), SST data from (https://cds.climate.copernicus.eu/datasets/satellite-sea-surface-temperature-ensemble-product?tab=overview).

Funding

This study did not obtain any precise allowance from funding activities in the community, profitable, or not-for-profit sectors.

Declaration of competing interest

The authors declare that they have no known competing financial interests or personal relationships that could have appeared to influence the work reported in this paper.

Acknowledgements

The authors thank the Director, INCOIS, for the facilities provided to accomplish this study. This is the INCOIS contribution number 601.

References

Ali, M.M., Jagadeesh, P.S.V., Lin, I.-I., Hsu, J.-Y., 2012. A neural network approach to estimate tropical cyclone heat potential in the Indian Ocean. IEEE Geosci. Remote Sens. Lett. 9 (6), 1114–1117.

Balachandran, S., Geetha, B., 2012. Development of a statistical model for predicting cyclone days over the North Indian Ocean. J. Earth Syst. Sci. 121 (5), 1187–1195. https://doi.org/10.1007/s12040-012-0211-x.

Camargo, S.J., Emanuel, K.A., Sobel, A.H., 2007. Use of a genesis potential index to diagnose ENSO effects on tropical cyclone genesis. J. Clim. 20 (19), 4819–4834. https://doi.org/10.1175/JCLI4282.1.

Chu, P.S., 2004. ENSO and tropical cyclone activity. In: Hurricanes and Typhoons: past, Present, and Future. Columbia University Press, pp. 297–332.

Ditchek, S.D., Carton, J.A., Stammer, D., 2016. Tropical cyclone heat potential and its relationship to oceanic heat content. Geophys. Res. Lett. 43 (2), 612–619. https://doi.org/10.1002/2015GL067559.

Emanuel, K.A., 1987. The dependence of hurricane intensity on climate. Nature 326, 483–485.

Emmanuel, R., Deshpande, M., Ganadhi, M.K., Ingle, S.T., 2021. Genesis of severe cyclonic storm Mora in the presence of tropical waves over the North Indian Ocean. Q. J. R. Meteorol. Soc. 147 (737), 2661–2678. https://doi.org/10.1002/qj.4113.

Ghetye, S., Nayak, A., 2020. Role of oceanic heat content and atmospheric interactions in tropical cyclone development: a case study in the North Indian Ocean. J. Mar. Sci. Eng. 8 (5), 323. https://doi.org/10.3390/jmse8050323.

Goni, G., Trinanes, J.A., 2009. Ocean heat content variability and tropical cyclone intensity in the North Atlantic. J. Phys. Oceanogr. 39 (7), 1738–1752. https://doi.org/10.1175/2009JPO4063.1.

Gray, W.M., 1979. Hurricanes: their formation, structure and likely role in the tropical circulation. In: Meteorology over the Tropical Oceans. Royal Meteorological Society, pp. 155–218.

Kotal, S.D., Kundu, P.K., Roy Bhowmik, S.K., 2009. Analysis of cyclogenesis parameter for developing and non-developing low-pressure systems over the North Indian Ocean. Nat. Hazards 50 (2), 389–402. https://doi.org/10.1007/s11069-008-9348-z.

Lin, I.I., Wu, C.C., Pun, I.F., Ko, D.S., Hsu, H.H., 2009. Upper-ocean thermal structure and the western North Pacific category-5 typhoons. Part I: ocean features and the category-5 typhoons' intensification. Monthly Weather Rev. 137 (1), 132–145. https://doi.org/10.1175/2008MWR2277.1.

Mall, R.K., Srivastava, A., Banerjee, T., 2019. Variability in tropical cyclone genesis over the Bay of Bengal during the post-monsoon season in a changing climate. Clim. Dyn. 53, 6201–6215. https://doi.org/10.1007/s00382-019-04794-1.

Maneesha, K., 2013. Role of Upper Ocean in the intensification and movement of tropical cyclones and their associated biogeochemical response in the Bay of Bengal Ph.D Thesis. Andhra University, Visakhapatnam India, p. 238.

Mohan, P.R., Srinivas, C.V., Yesubabu, V., Rao, V.B., Vittal Murthy, K.P.R., Venkatraman, B., 2022. Impact of SST on the intensity prediction of extremely severe tropical cyclones Fani and Amphan in the Bay of Bengal. Atmos. Res. 273, 106151. https://doi.org/10.1016/j.atmosres.2022.106151.

Mohanty, S., Nadimpalli, R., Osuri, K.K., Pattanayak, S., Mohanty, U.C., Sil, S., 2019. Role of sea surface temperature in modulating life cycle of tropical cyclones over Bay of Bengal. Trop. Cycl. Res. Rev. 8 (2), 68–83.

Mohapatra, M., Mandal, G.S., Bandyopadhyay, B.K., Tyagi, A., Mohanty, U.C., 2012. Classification of cyclone hazard prone districts of India. Nat. Hazards 63, 1601–1620. https://doi.org/10.1007/s11069-011-9923-5.

Murakami, H., Wang, B., 2010. Future change of North Atlantic tropical cyclone genesis frequency and the role of the African easterly waves. J. Clim. 23 (11), 2699–2718. https://doi.org/10.1175/2010JCLI3541.1.

Naresh Krishna, K., Bhaskar Rao, D.V., 2013. Numerical study of ocean–atmosphere coupling on tropical cyclone intensity. Meteorol. Atmos. Phys. 119 (1-2), 29–44. https://doi.org/10.1007/s00703-012-0217-3.

Nellipudi, N.R., Viswanadhapalli, Y., Challa, V.S., Vissa, N.K., Langodan, S., 2021. Impact of surface roughness parameterizations on tropical cyclone simulations over the Bay of Bengal using WRF-OML model. Atmos. Res. 262, 105779. https://doi.org/10.1016/j.atmosres.2021.105779.

Nicholls, N., 1984. The Southern Oscillation, sea surface temperature, and interannual fluctuations in Australian tropical cyclone activity. J. Climatol. 4 (6), 661–670. https://doi.org/10.1002/joc.3370040606.

Nicholls, N., 1992. Recent performance of a method for forecasting Australian seasonal tropical cyclone activity. Aust. Meteorol. Mag. 40 (2), 105–110.

Pun, I.-F., Lin, I.-I., Lo, M.-H., 2013. Recent increase in high tropical cyclone heat potential area in the Western North Pacific Ocean. Geophys. Res. Lett. 40 (17), 4680–4684.

Ramakrishna, S.S.V.S., Rao, N.N., Ravi Srinivasa Rao, B., Srinivasa Rao, P., Srinivas, C.V., Dasari, H.P., 2019. Impact of moisture transport and boundary layer processes on a very severe cyclonic storm using the WRF model. Pure Appl. Geophys. 176 (12), 5445–5461.

Rao, N.N., Rao, V.B., Ramakrishna, S.S.V.S., 2019. Moisture budget of the tropical cyclones formed over the Bay of Bengal: role of soil moisture after landfall. Pure Appl. Geophys. 176 (2), 441–461. https://doi.org/10.1007/s00024-018-1964-0.

Revell, C.G., Goulter, S.W., 1986. South Pacific tropical cyclones and the Southern Oscillation. Monthly Weather Rev. 114 (6), 1138–1145. https://doi.org/10.1175/1520-0493(1986)114<1138:SPTCAT>2.0.CO;2.

Roy Bhowmik, S.K., 2003. An objective technique for determining genesis potential zone of tropical cyclones over the Indian seas. Curr. Sci. 85 (1), 71–74.

Sadhuram, Y., Ramana, Murthy, T.V., Somayajulu, Y.K., 2006. Estimation of tropical cyclone heat potential in the Bay of Bengal and its role in the genesis and intensification of storms. Indian J. Marine Sci. 35 (2), 132–138.

Shay, L.K., Goni, G.J., Black, P.G., 2000. Effects of a warm oceanic feature on Hurricane Opal. Monthly Weather Rev. 128 (5), 1366–1383. https://doi.org/10.1175/1520-0493(2000)128<1366:EOAWOF>2.0.CO;2.

Shay, L.K., Uhlhorn, E.W., Black, P.G., Franklin, J.L., 2011. Observations of oceanic thermal structure in the Bay of Bengal during Cyclone Nargis. J. Phys. Oceanogr. 41 (9), 1757–1779. https://doi.org/10.1175/2011JPO4437.1.

Singh, N., Mohanty, U.C., Pradhan, M.R., 2020. Influence of ocean heat content and sea surface temperature on tropical cyclone genesis and intensification over the BoB. Meteorol. Atmos. Phys. 132 (4), 513–532. https://doi.org/10.1007/s00703-020-00732-2.

Suneeta, P., Ramakrishna, S.S.V.S., 2021. Modified tropical cyclone genesis potential index over the Bay of Bengal during southwest and post-monsoon seasons. J. Earth Syst. Sci. 130 (4), 196.

Suneeta, P., Sadhuram, Y., 2018. Tropical cyclone genesis potential index for Bay of Bengal during peak post-monsoon (October-November) season including atmosphere-ocean parameters. Mar. Geodesy 41 (1), 86–97.

Wu, L., Wang, B., Braun, S.A., 2007. Impacts of the Saharan air layer on hurricane intensity. Geophys. Res. Lett. 34 (9), L09802. https://doi.org/10.1029/2007GL029564.

Zhang, H., Lian, L., Ma, L., Chen, S., 2016. Ocean heat content variability and its relationship with tropical cyclone intensity over the western North Pacific. J. Geophys. Res. Oceans 121 (7), 5155–5170. https://doi.org/10.1002/2016JC011852.